

A bar in the inner halo of barred galaxies I. Structure and kinematics of a representative model

E. Athanassoula

Laboratoire d'Astrophysique de Marseille, Observatoire Astronomique de Marseille Provence, 2 Place Le Verrier, F-13248 Marseille Cedex 4, France

Accepted . Received ;

ABSTRACT

N-body simulations argue that the inner haloes of barred galaxies should not be spherical, nor even axisymmetric, but triaxial. The departure from sphericity is strongest near the centre and decreases outwards; typical axial ratios for the innermost parts are of the order of 0.8. The halo shape is prolate-like in the inner parts up to a certain radius and then turns to oblate-like. I call this inner halo structure the ‘halo bar’ and analyse here in depth its structure and kinematics in a representative model. It is always considerably shorter than the disc bar. It lags the disc bar by only a few degrees at all radii and the difference between the two bar phases increases with distance from the centre. The two bars turn with roughly the same pattern speed. This means that the halo bar is a slow bar, since its corotation radius is much larger than its length. The bisymmetric component in the halo continues well outside the halo bar in the form of an open spiral, trailing behind the disc bar. The inner parts of the halo display some mean rotation in the same sense as the disc rotation. This is more important for particles nearer to the equatorial plane and decreases with increasing distance from it, but is always much smaller than the disc rotation.

Key words: galaxies: evolution – galaxies : haloes – galaxies: structure – galaxies: kinematics and dynamics – methods: numerical.

1 INTRODUCTION

The exchange of angular momentum between different parts of a barred galaxy is of major importance for its evolution. Lynden-Bell & Kalnajs (1972) first discussed this process in the case of a spiral galaxy. Their paper was followed by a number of others, discussing and establishing the role of angular momentum exchange for various aspects of disc galaxy evolution (Mark 1976; Kormendy 1979; Sellwood 1980; Tremaine & Weinberg 1984; Weinberg 1985; Tagger *et al.* 1987; Sygnet *et al.* 1988; Little & Carlberg 1991a; 1991b; Hernquist & Weinberg 1992; Athanassoula 1996; Debattista & Sellwood 2000; Athanassoula 2002, hereafter A02; Weinberg & Katz 2002; Athanassoula 2003, hereafter A03; Valenzuela & Klypin 2003; Fuchs 2004; Athanassoula 2005b; Fuchs & Athanassoula 2005; Holley-Bockelmann, Weinberg & Katz 2005; Debattista *et al.* 2006; Martinez-Valpuesta, Shlosman & Heller 2006). Most of these studies are based on *N*-body simulations.

Lynden-Bell & Kalnajs (1972) showed that angular momentum is transferred from the inner to the outer parts of the disc and that it is mainly (near)-resonant material that will emit, or absorb it. Material at inner Lindblad resonance (hereafter ILR) will lose angular momentum, while material at corotation (hereafter CR) and outer Lindblad resonance (hereafter OLR) will gain it. Spiral structure within CR is a disturbance with negative angular momentum, so that feeding it with angular momentum will damp it, while

taking angular momentum from it will excite it (see also Kalnajs 1971).

This insightful analytical picture did not include any spheroidal component. It was thus extended later in the context of bar slow down by Tremaine & Weinberg (1984), Weinberg (1985) and Hernquist & Weinberg (1992), and in the context of bar growth by A02 and A03. The halo has a different behaviour from that of the disc, since, provided the halo distribution function is a function of the energy only, it is possible to show that halo particles at all resonances will gain angular momentum. It should be possible to extend this property to a more general class of distribution functions, provided energy is the main functional dependence and an appropriate perturbation expansion can be used. If both the outer disc and the halo can absorb angular momentum, then the inner disc can emit more than it would in the absence of a halo, and this, since the bar is a negative angular momentum ‘perturbation’, will lead to a stronger bar than if only the outer disc is absorbing (A02; A03). This means that stronger bars can be found in models whose haloes have higher densities in the resonance regions, and thus explains the results found by Athanassoula & Misiriotis (2002, hereafter AM02).

As the bar loses angular momentum it will grow stronger (A02; A03) and will also slow down, i.e. its pattern speed will decrease (Weinberg 1985; Little & Carlberg 1991a,b; Hernquist & Weinberg 1992; Athanassoula 1996; Debattista & Sellwood 2000;

2 A bar in the inner halo of barred galaxies I

A03; O'Neill & Dubinski 2003; Martinez-Valpuesta *et al.* 2006). The amount of angular momentum gained/lost at a given resonance depends on the density there, but also on how cold the material at resonance is (A03), since colder material can emit/absorb much more angular momentum than hot material. Thus, these two factors determine the angular momentum exchange and therefore the morphology, strength and angular velocity of the bar (A03; Athanassoula 2005b).

Although a number of studies have addressed the effect of the bar evolution on the disc component (e.g. Debattista & Sellwood 2000; AM02; A02; A03; O'Neill & Dubinski 2003; Valenzuela & Klypin 2003; Martinez-Valpuesta & Shlosman 2004; Holley-Bockelmann *et al.* 2005; Debattista *et al.* 2006; Martinez-Valpuesta, Shlosman & Heller 2006), very few have focused on the effect on the halo component. Most of these address the effect of the bar on the halo radial density profile (Hernquist & Weinberg 1992; Weinberg & Katz 2002; Sellwood 2003; Athanassoula 2004; Holley-Bockelmann *et al.* 2005; McMillan & Dehnen 2005; Sellwood 2006), while a few address other aspects of the halo evolution. Debattista & Sellwood (2000) mentioned an induced bisymmetric distortion in the halo. A02 showed that a considerable fraction of the halo particles is at resonance with the bar. In particular at CR, but also at ILR, OLR and at several other resonances. This was further confirmed in A03, where it was also shown that, as predicted analytically for distribution functions that depend on the energy only, the halo resonances absorb angular momentum. Further confirmation, for different models and/or with different techniques have been also given by Ceverino & Klypin (2005) and by Martinez-Valpuesta *et al.* (2006). O'Neill & Dubinski (2003) also discussed the existence of a bar in the halo component and mentioned an axis ratio of 0.88. A bar in the halo component is shown in fig. 2 of Holley-Bockelmann *et al.* (2003). Various aspects of the effect of a non-axisymmetric halo on bar evolution were discussed by El-Zant & Shlosman (2002), Berentzen, Shlosman & Jogee (2006), Berentzen & Shlosman (2006) and Heller, Shlosman & Athanassoula (2007).

Three works discussed properties of the halo bar in some detail. Hernquist & Weinberg (1992) were the first to discuss the halo bar and gave axial ratio values of 0.7 and 0.8-0.9 for c/a and b/a , respectively. They also mentioned that the halo bar lags the disc bar somewhat. CPU limitations at the time, however, made them use a live halo but a rigid bar and no disc. Thus, their results do not include the effect of the bar evolution on the halo properties. As mentioned by the authors, this work needs to be extended to cover a broader part of the parameter space and, particularly, to include a live disc. Athanassoula (2004; 2005b; 2005c) discussed briefly some halo bar properties, including the increase of the bar length with time. The third of these papers discusses also the orbital structure in the halo, including the chaos versus regularity question and the properties of the near-resonant orbits. Finally, Colin, Valenzuela & Klypin (2006) discuss the properties of the halo bar, which they call 'dark matter bar', in cosmologically motivated simulations and find properties in agreement with those in Athanassoula (2004; 2005b; 2005c). In particular, they give an axial ratio of 0.7.

Here I will extend previous studies and discuss in depth the properties of the halo bar in a number of high resolution, fully self-consistent N -body simulations. This paper is the first of a set, where I discuss the effects of the disc bar and of its evolution on the halo component. In § 2, I briefly summarise some relevant information on all the simulations, both the one discussed here and those discussed in the second paper of this series (Paper II). In particular, I describe the different types of initial conditions used. In

§ 3, I introduce the halo bar. Its shape and length are discussed in § 3.1 and 3.2. In § 4, I introduce spherical harmonics to measure the halo bar properties and in particular its strength, length and position angle. Kinematics are discussed in § 5 and I briefly summarise in § 6. A discussion of the implications of the results of this paper will be given in Paper II, after I discuss the time evolution of the halo bar properties and present statistics from a large sample of several hundred simulations.

2 SIMULATIONS

In this work, I consider simulations with a large variety of initial conditions. In order to allow comparisons, however, all models share a few common features. In particular, all the models are composed of a disc, a halo, and sometimes also a bulge component. The disc has an initial volume density profile

$$\rho_d(R, z) = \frac{M_d}{4\pi R_d^2 z_0} \exp(-R/R_d) \operatorname{sech}^2(z/z_0), \quad (1)$$

where R is the cylindrical radius, M_d is the disc mass and R_d and z_0 are the disc radial and vertical scale-lengths, respectively. In all cases $M_d = 1$ and $R_d = 1$. This allows me to compare the results of the various simulations directly, without any rescaling. I consider five families of simulations, with different initial conditions for the spheroid.

The first family has the halo and bulge radial profiles described in Hernquist (1993) and used in AM02, A02 and A03 and is called here for brevity the AM family. The initial halo density profile is

$$\rho_h(r) = \frac{M_h}{2\pi^{3/2}} \frac{\alpha}{r_c} \frac{\exp(-r^2/r_c^2)}{r^2 + \gamma^2}, \quad (2)$$

where r is the spherical radius, M_h is the halo mass and γ and r_c are the halo scale-lengths. γ can be considered as the core radius of the halo. The constant α is defined by

$$\alpha = [1 - \sqrt{\pi} q \exp(q^2) (1 - \operatorname{erf}(q))]^{-1},$$

where $q = \gamma/r_c$ (Hernquist 1993). If a particularly extended halo is necessary, the halo radial density profile is described by the sum of two densities of the kind given by Eq. 2.

As shown in AM02 and as explained in A02 and A03, the size of the halo core strongly influences the bar evolution. Haloes with a small core have a lot of mass in the inner regions and thus, provided their velocity dispersion is not too high, they can contribute substantial angular momentum sinks and lead to considerable angular momentum exchange between the near-resonant particles in the bar region and the near-resonant particles in the halo. Such models grow strong bars, i.e. bars that are long, thin and massive and have rectangular-like isodensities (AM02). Viewed side-on, i.e. edge-on with the line-of-sight along the bar minor axis, they exhibit a strong peanut, or even X-like shape. Such models are termed MH in the above mentioned works. On the contrary, haloes with large cores have considerably less material in the inner parts and lead to less angular momentum exchange. They are termed in the above mentioned works as MD. Bars grown in such environments are less strong, have elliptical-like isodensities when viewed face-on and boxy-like when viewed side-on. More on the properties of these bars, their different evolution and the explanation of these differences can be found in AM02, A02, A03 and Athanassoula (2005a; 2005b). Let me stress, however, that there is no discontinuity between the two types of models. On the contrary, MH and MD types

are the two extremes of a continuous sequence, based on a continuous distribution of core sizes and of amount of angular momentum exchanged.

The AM models sometimes have also a bulge component. Whenever present, this has an initial density profile

$$\rho_b(r) = \frac{M_b}{2\pi a_b^2} \frac{1}{r(1+r/a_b)^3}, \quad (3)$$

where M_b is the bulge mass and a_b is the bulge scale-length. I will hereafter refer to this as the Hernquist profile (Hernquist 1990).

The adding of the disc and spheroidal components together is not trivial and I will describe here the three methods I used when building the various AM models. I first make the spheroidal component (halo plus, when present, bulge) so that it is in equilibrium in its own potential plus the monopole term of the disc potential (i.e. the spherically symmetric equivalent of the disc). In the initial conditions built following Hernquist (1993), this spheroid is simply stacked on the disc component. Thus the simulation starts somewhat off equilibrium, but settles after only a few transients. A second method consists in first finding an equilibrium by running a constrained simulation in which the spheroid and disc components are constrained to stay axisymmetric. Once this is achieved, the full unconstrained simulation can start with initial conditions either the previously found equilibrium, or with disc velocities modified so as to follow given constraints, e.g. a given profile of the Q stability parameter (Toomre 1964). In the third method I grow the remaining terms (above the monopole) of the disc potential adiabatically in the spheroid, thus allowing it to settle to a new equilibrium, as e.g. in McMillan, Athanassoula & Dehnen (2007) and in McMillan & Dehnen (2007). I then remove the disc potential and introduce the disc particles. In both the second and the third method the simulation starts very near equilibrium. Obviously, in all three methods, the initial conditions are not exactly as described by Eqs. 1, 2 and 3, since the components have interacted between them and adjusted to each other. Furthermore, the adjustments in the three methods are not identical, as expected. Nevertheless, and this is important to stress, the simulations starting from these three methods give the same global behaviour, evolution and trends. More information on how the disc component was set up can be found in Hernquist (1993), in AM02 and in A03.

I also included in this study three families of initial conditions with a cuspy halo. In the first, the AM2 family, the initial halo profile is as in Eq. 2 with γ of the order of 10^{-2} . In the second, the HRN family, the halo has initially a Hernquist profile (Eq. 3). Finally in the third family, the McM family, I used the initial conditions described by McMillan & Dehnen (2007). For these simulations the halo has initially a profile:

$$\rho_h(r) = \frac{\rho_c}{(r/r_h)^{\gamma_0}(1+r/r_h)^{3-\gamma_0}} \text{sech}(r/r_t), \quad (4)$$

where ρ_c is a density scale, r_h is the halo scale radius, r_t is the halo truncation radius and γ_0 measures the inner slope of the density profile. As in the previous families of models, the bulge here, whenever present, has initially a Hernquist (1990) radial profile. The halo distribution function is built using the Cuddeford (1991) inversion, while that of the disc uses the method of Dehnen (1999).

I also ran simulations with the initial conditions of Kuijken & Dubinski (1995), which constitute the KD family. In these models, the bulge follows a King (1966) model and the halo has a low-ered Evans distribution function (Kuijken & Dubinski 1994). The distribution function of the disc is a three-dimensional generalisation of the planar distribution function of Shu (1969) and Kuijken

& Tremaine (1992) and the radial density profile on the equatorial plane is very near exponential. The Kuijken & Dubinski (1995) model also allows one to start with a flattened or with a rotating halo and I have used this in a few cases.

In most of the simulations, all the particles have the same mass. However, in a couple of dozen simulations of the AM family the outer halo particles have a larger mass. As discussed in A03, the largest masses are attributed to particles with the largest pericenters, thus ensuring that these particles will not reach the inner regions. Of course the halo distribution will change with time, but by being sufficiently cautious about the pericenter limits, one can make sure that the high mass particles will not reach the disc radii. In most simulations of the McM family, I followed the precepts of McMillan *et al.* (2007) and McMillan & Dehnen (2007) and used halo particles with four times the mass of the disc particles and halo softening twice as large as that of the disc particles. Thus the maximum force exerted by a single particle ($\propto m_i/\epsilon_i^2$, where m_i and ϵ_i the mass and softening of the particle, respectively) is the same for all particles.

Some of these simulations were run on our GRAPE-5 systems (Kawai *et al.* 2000), while the others used the public version of W. Dehnen's treecode (Dehnen 2000; 2002). As already discussed in A03, the results obtained with the two codes are in very good agreement. In most simulations the disc has 200 000 particles and the halo about a million. I also ran several simulations with a considerably larger number of particles. In all simulations the gravitational constant $G = 1$.

The representative simulation discussed here is part of the AM family with the non-monopole terms of the disc potential grown adiabatically in the spheroid (last of the three methods described above) and has $z_0 = 0.2$, $Q = 1.2$, $M_h = 5$, $\gamma = 0.5$, $r_c = 10$ and $M_b = 0$, i.e. is of MH type. All plots and results, unless otherwise stated, refer to time $t = 800$, i.e. a time towards the end of the simulations, well in the secular evolution regime. Like in most simulations, the number of particles in the disc is 200 000 and about a million in the halo. This is sufficient for a good description of the evolution, but can give relatively noisy isodensity contours in a plot. In order to obtain smooth isocontours without smoothing or loss of information, I used in Figs. 1 to 3 the technique described in Athanassoula (2005a). In Paper II, I will discuss statistics from all families of models presented here.

In order to convert computer units to units more readily used when describing galaxies, I need to set the units of length and mass to values representative of a barred galaxy. AM02 used a length unit of 3.5 kpc and a mass unit of $5 \times 10^{10} M_\odot$. This choice, however, is in no way unique, and I can choose quite different values. Because of this, I will not adopt here any particular calibration, but stick to computer units. The reader can easily convert units according to his/her needs and the objects under consideration.

3 THE HALO BAR

Fig. 1 shows the three orthogonal views of the disc component of the representative simulation at time 800. Only the inner part is shown, in order to show best the bar. Seen face-on, this has isodensities which are elliptical-like in the inner parts and rectangular-like further out. The bar is surrounded by a ring, as the inner rings often seen in barred galaxies. Seen side-on, the inner disc shows a strong peanut feature, again as often observed. This is called by observers a peanut bulge. Seen end-on, i.e. edge-on with the line of sight along the bar major axis, the bar contributes a spherical-

4 A bar in the inner halo of barred galaxies I

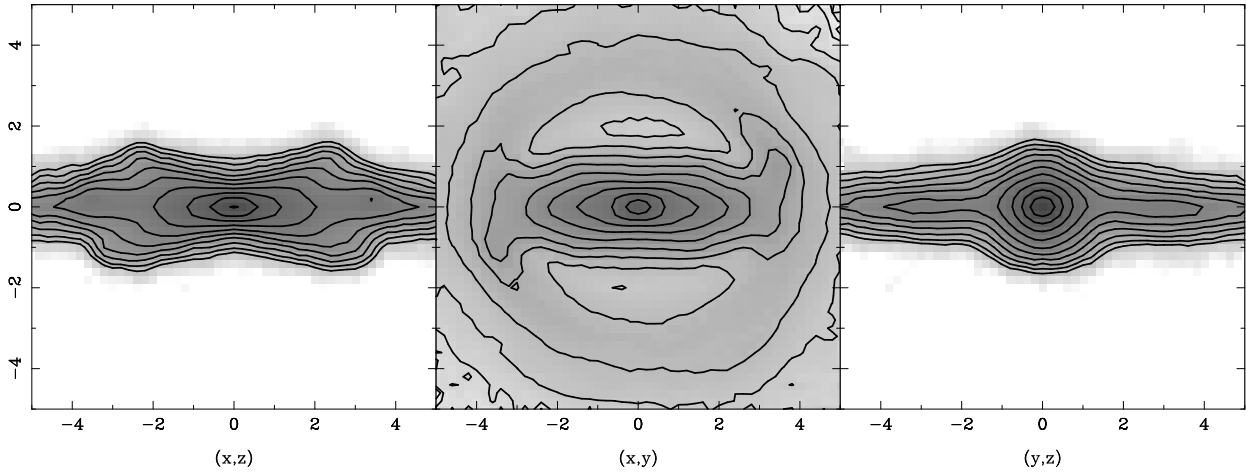


Figure 1. Three orthogonal views of the disc component. The left panel gives the edge-on side-on view, the right one gives the edge-on end-on view and the middle one the face-on view. The projected density of the disc is given by grey-scale and also by isocontours (spaced logarithmically).

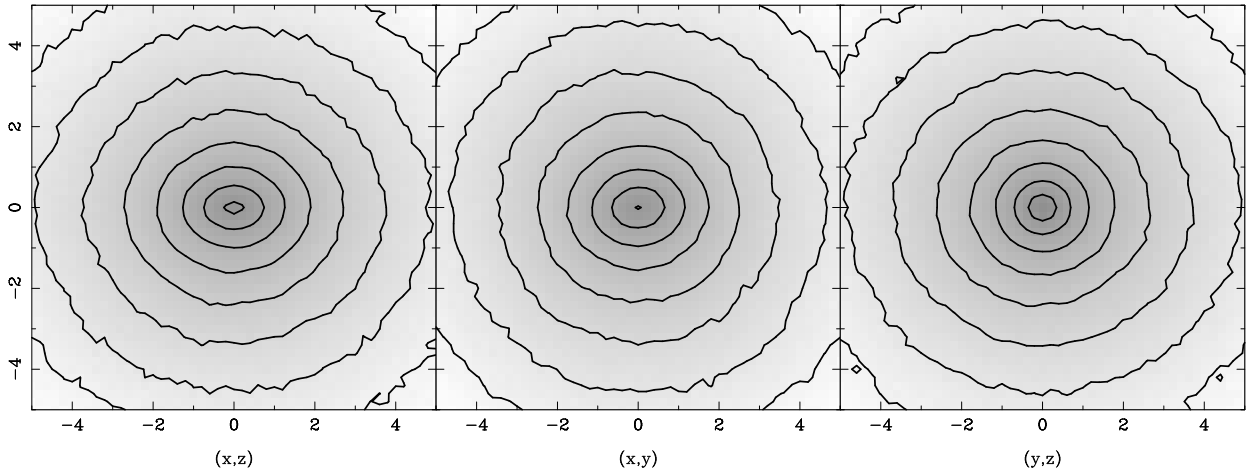


Figure 2. As for Fig. 1, but for the halo component.

like central feature. This has the same aspect as observed classical bulges in so called non-barred galaxies (for a discussion of bulge types see Athanassoula 2005a).

Fig. 2 shows the three corresponding orthogonal views of the halo component. It is clear that the halo distribution is not spherical. Particularly in the inner parts, it has a prolate-like shape and seems to become less elongated at larger radii. It also seems that the shortest axis is perpendicular to the disc equatorial plane and the longest along the major axis of the disc bar. For simplicity, I will call this elongated feature in the centre of the halo component the halo bar, although its shape is more reminiscent of an oval. It is definitely less strong than the disc bar, less eccentric and also shorter. Seen side-on it never has a peanut shape. Its shape in all three projections looks roughly elliptical, so that the three-dimensional shape can be described as ellipsoidal. It looks roughly aligned with the disc bar. All these statements will be made more quantitative in the next sections.

Fig. 2 has been made as Fig. 1, i.e. I projected all the matter on the equatorial plane. However, since the halo shape is triaxial in the inner parts and very near spherical in the outer parts, this projection will make isodensities more round than the true three dimensional shape. For this reason, I plot in Fig. 3 again the isodensities, but this time taking into account only particles with $|z| < 1$. A comparison

of Figs. 2 and 3 shows that the difference is small. This is due to the fact that the halo is fairly concentrated, so that the density in the outer parts is much lower than in the inner parts.

3.1 Halo inertia tensor and the axial ratio of its bar

Since the shape of the bar is roughly ellipsoidal, I used the inertia tensor to calculate its axial ratio. For this I first assigned a local density to each halo particle, by calculating the distance to its nearest neighbours (Casertano & Hut 1985) with the help of the NEMO package (Teuben 1995). The particles were sorted in order of increasing local density and divided in groups with local densities within a given range, discarding those with the highest densities to ensure that the distribution is not influenced by the softening. The axial ratios for each group are obtained (e.g. Barnes 1992) as those of the homogeneous ellipsoid that has the same moment of inertia as the particle distribution. Tests showed that, if the sorting is done with respect to the distance of the particles from the centre, then a bias towards sphericity is introduced, since the shells into which the particles are divided are necessarily spherical. A similar bias, although less strong, is introduced if the particles are sorted by their potential or by their binding energy, since the corresponding isocontours are more spherical-like than the density ones. I adopted

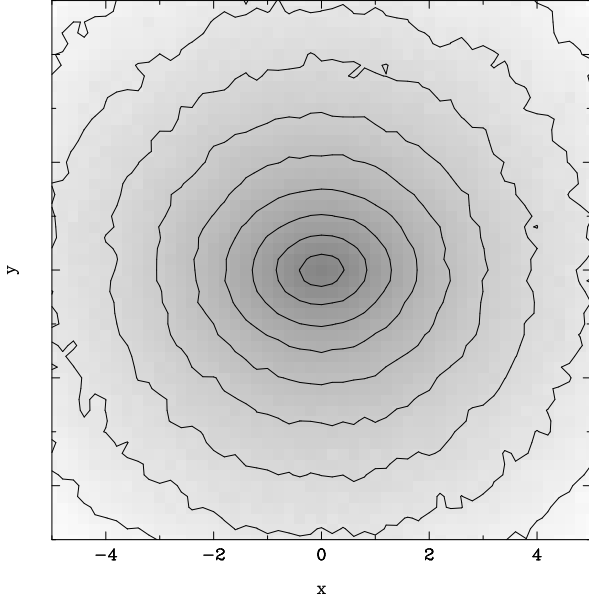


Figure 3. (x, y) view of the halo projected density. As for Fig. 2, but the projected surface density is now obtained only from the mass within a slice around the disc equatorial plane, i.e. is based only on particles with $|z| < 1$.

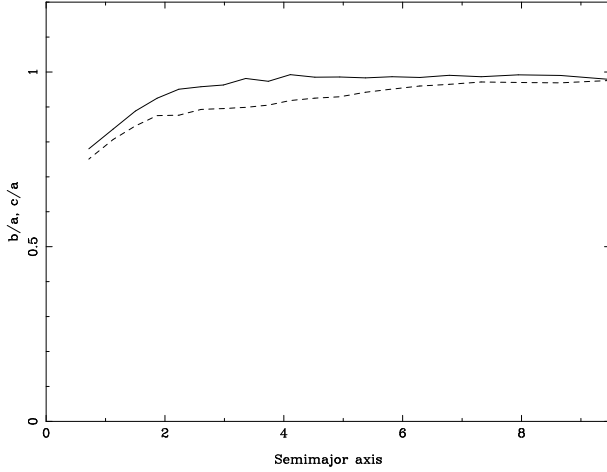


Figure 4. Axial ratios as a function of semimajor axis for the halo mass distribution. The b/a ratio is given with a full line and the c/a by a dashed line.

here a sorting by density since a number of tests showed me that this does not introduce any bias and gives very satisfactory results, its only disadvantage being that it is rather CPU intensive.

I thus obtain $b/a = \sqrt{(q_2/q_1)}$ and $c/a = \sqrt{(q_3/q_1)}$, where q_1, q_2 and q_3 are the eigenvalues of the inertia tensor, a, b and c are the lengths of the three principal semi-axes of the halo and $a > b > c$. Their ratios are plotted in Fig. 4 as a function of the average semimajor axis of the shell. The parts within roughly four initial disc scale-lengths depart substantially from sphericity, and more strongly so for regions nearer to the centre. The innermost group of particles has axis ratios somewhat less than 0.8. Within roughly the first 2 initial disc scale-lengths, the two axial ratios do not differ substantially, i.e. the general shape, although triaxial, is not far from prolate. Somewhat further out and up to roughly 6 initial disc scale-lengths b/a is very near unity, while c/a is smaller. Thus, the shape

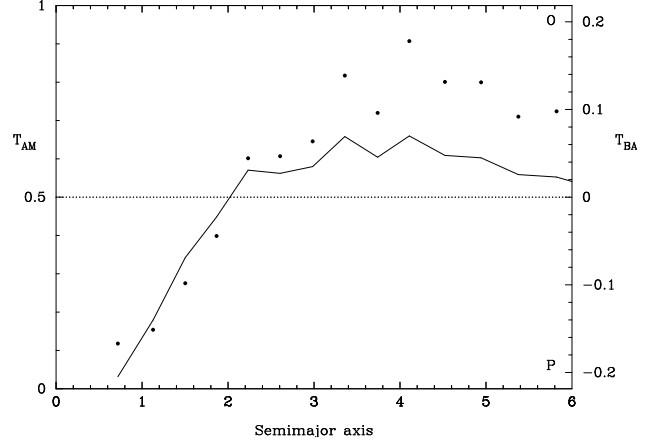


Figure 5. Triaxiality parameters T_{AM} (filled circles, ordinate to the left of the panel) and T_{BA} (solid line, ordinate to the right of the panel) as a function of semimajor axis for the halo component. For both measures of triaxiality, the region above the dotted horizontal line corresponds to oblate-like configurations and the region below it to prolate-like ones.

is more oblate-like in this region. This is better seen from measures of the triaxiality discussed below.

In Fig. 5, I plot the triaxiality of the halo component. Several definitions have been used so far. Aguilar & Merritt (1990) use

$$T_{AM} = \frac{b - c}{a - c}. \quad (5)$$

T_{AM} takes values in the range $[0, 1]$, where the lower bound corresponds to a prolate shape and the upper one to an oblate one. As explained, however, in Boily & Athanassoula (2006), T_{AM} is sensitive to noise and to the corresponding small errors in the calculation of the axes if $a \sim b \sim c$. To avoid this, Boily & Athanassoula use

$$T_{BA} = \frac{b^2 - c^2}{b^2 + c^2} - \frac{a^2 - b^2}{a^2 + b^2}. \quad (6)$$

This takes values in the range $[-1, 1]$ and is positive for oblate shapes and negative for prolate ones.

The results of these two definition are compared in Fig. 5. Obviously, one should not compare the numerical values given by the two definitions, since the two mathematical forms are different. One should compare the general form of the profile and the ranges where the two say that the form is oblate-like, or prolate-like. Therefore, Fig. 5 shows that the two definitions agree well. The structure is prolate-like from the centre to a semimajor axis ~ 2 . Beyond that and up to 6 the configuration is roughly oblate-like, with a maximum oblateness for a semimajor axis around 4. Beyond 6 the configuration is too near-spherical for any of the two methods to be able to assess its shape (see also Fig. 4).

3.2 Ellipse fitting and projected axial ratio of the halo bar

As the shape of the disc bar is far from ellipsoidal, AM02 did not use the inertia tensor in order to measure the bar axial ratio in the equatorial plane. Instead, they used the method introduced by Athanassoula *et al.* (1990) for observations. Namely, they projected the density on the equatorial plane and fitted generalised ellipses to the isodensities. The equation of the generalised ellipse, initially introduced by Athanassoula *et al.* (1990), is

$$(|x|/a)^\lambda + (|y|/b)^\lambda = 1, \quad (7)$$

where a and b are the semimajor and semiminor axes, respectively,

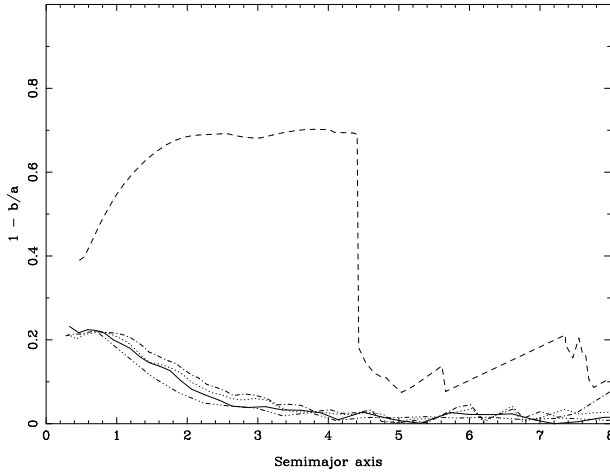


Figure 6. Ellipticity in the equatorial plane of the bar in the disc and the halo components. The dashed line gives results from ellipse fits to the disc density projected on the equatorial plane. The solid line corresponds to ellipses fitted similarly to the whole halo, the dot-dashed line to the halo truncated at $|z| < 1$ and the dotted line to the halo truncated at $|z| < 2$. The dashed-triple-dot line gives the results from the halo inertia tensor.

and λ is a parameter describing the shape of the generalised ellipse. For $\lambda=2$ the shape is a standard ellipse, for $\lambda < 2$ it is a lozenge, while for $\lambda > 2$ it approaches a rectangle, and, for simplicity, is generally called rectangular-like.

In Fig. 6, I plot the ellipticity $1 - b/a$ of the disc and of the halo components, obtained as described above. The profile for the disc resembles that shown in the upper left panel of Fig. 4 of AM02, as could be expected, since both results are obtained for MH-type bars. It has a relatively flat part and then drops abruptly at a semimajor axis of ~ 4.4 . It thus provides one of the possible ways of measuring the bar length for a strong bar (AM02). The halo bar presents a totally different profile. The axial ratio increases slowly inwards either steadily, or reaching at small radii a plateau of short extent. Contrary to the disc bar, it has no sharp increase or decrease that could help determine the bar length. I can, nevertheless, distinguish two separate parts to the profile, one in which the ellipticity decreases with radius and the other where it is consistent with zero, to within the noise. The transition occurs at a radius between 3 and 4.4 length units, i.e. within the disc bar length, but a sharper evaluation is not possible. Furthermore, this length is not necessarily equal to the halo bar length, but just constitutes an upper limit. To define the halo bar length one needs to measure the phase of the $m=2$ component as will be done in § 4. Here, I can just conclude that the halo bar length can not exceed an upper limit, estimated between 3 and 4.4 length units, i.e. can not exceed the length of the disc bar. Fig. 6 also shows that the halo bar is much less elongated than the disc bar, as could already be inferred by a comparison of Figs. 1 and 2. E.g., at a distance of two initial disc scale-lengths the ellipticity of the halo bar is about seven times that of the disc bar.

In the above, I treated the halo bar in exactly the same way as the disc bar, i.e. I first projected the density on the disc equatorial plane. Although this is a reasonable thing to do for the disc, it is less appropriate for haloes, since these extend roughly the same in all directions and thus a projection on the equatorial plane may artificially circularise the isodensities, particularly in the inner regions. For this reason, I repeated this ellipse fitting, but now truncating the halo so that particles with $|z| > 1$, or $|z| > 2$, are ignored. The results are also shown in Fig. 6. Note that the difference is not large,

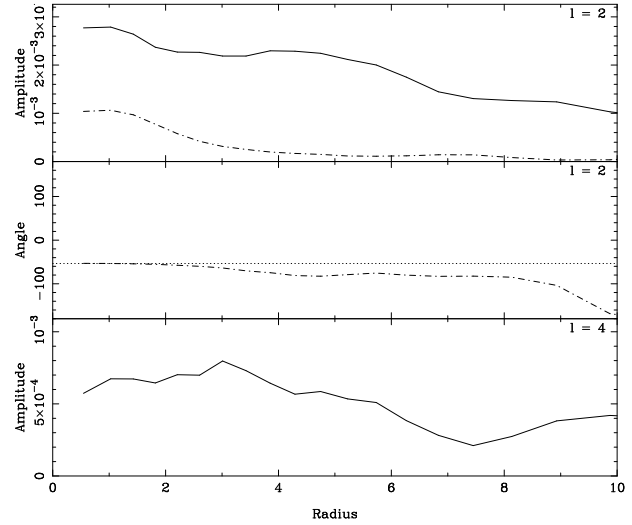


Figure 7. Results of the spherical harmonic expansion of the halo mass. The upper panel gives the amplitude of the $l=2$ components. The $m=0$ component is given with a full line and the $m=2$ one with a dot-dashed line. The middle panel gives the $l=2$ $m=2$ phase angle with a dot-dashed line and the position angle of the disc bar with a dotted line. The lower panel gives the amplitude of the $l=4$, $m=0$ component.

so that one can get estimates of the halo bar axial ratio from any of these three measurements. As already mentioned, this must be due to the fact that the halo is centrally concentrated, so that its density falls rapidly with distance from the centre.

In § 3.1 I measured the halo bar ellipticity using the inertia tensor of the three dimensional halo mass distribution. Although this method is conceptually the most correct one, it has a clear drawback. Namely, a relatively large number of particles are needed in order to estimate the axial ratio of the inner parts and as a consequence the innermost measurement can not be very near the centre. The ellipse fitting method discussed here does not share this disadvantage, so it gives information for much smaller radii. Fig. 6 compares the results of the two methods and shows that they agree well, a welcome result, since it allows the use of either method for statistical measurements, such as will be given in Paper II. Note that the innermost measurement from the inertial tensor is at ~ 0.8 length units, while the innermost from the fitted generalised ellipses is at ~ 0.4 length units.

4 SPHERICAL HARMONIC ANALYSIS

In order to measure the strength of the disc bar it is customary, both for observations and for simulations, to Fourier analyse the face-on density distribution (e.g. Ohta, Hamabe & Wakamatsu 1990; Ohta 1996; AM02; Laurikainen *et al.* 2006; Buta *et al.* 2006). This method, however, is not appropriate for the halo, which has a three-dimensional density distribution. Instead, I expand the density, $\rho(r, \theta, \phi)$, in spherical harmonics

$$\rho(r, \theta, \phi) = \sum_{l=0}^{\infty} \sum_{m=-l}^l \rho_{lm} Y_l^m(\theta, \phi), \quad (8)$$

where ϕ is the azimuthal angle and θ is the meridional angle, i.e. measured from the z axis. Y_l^m denotes the spherical harmonics defined as

$$Y_l^m(\theta, \phi) = \sqrt{\frac{2l+1}{4\pi} \frac{(l-|m|)!}{(l+|m|)!}} \times P_l^{|m|}(\cos \theta) e^{im\phi} \begin{cases} (-1)^m & \text{if } m \geq 0 \\ 1 & \text{if } m < 0 \end{cases} \quad (9)$$

and

$$Y_l^{-m}(\theta, \phi) = (-1)^m Y_l^{m*}(\theta, \phi), \quad (10)$$

so that

$$\rho_{lm}(r) = \int_0^\pi \int_0^{2\pi} d\phi Y_l^{-m*}(\theta, \phi) \rho(r, \theta, \phi), \quad (11)$$

where the $*$ denotes a complex conjugate.

The density of a sum of point masses can be written as

$$\rho(r, \theta, \phi) = \sum_k \frac{m_k}{r_k^2} \delta(r - r_k) \delta(\phi - \phi_k) \delta(\cos \theta - \cos \theta_k), \quad (12)$$

where the index k denotes the particle and r_k , ϕ_k , θ_k and m_k are its radius, angle coordinates and mass, respectively. The volume density, however, is not well adapted to N -bodies; instead it is more convenient to work with the mass in a spherical shell. Using Eqs. 11 and 12 and integrating over the radius in a spherical shell centred at radius r , I find

$$M_{lm}(r) = \sum_i m_i Y_l^{-m*}(\theta_i, \phi_i), \quad (13)$$

where the summation is carried over all particles in the shell and where r_i , θ_i and ϕ_i are the radius and angle coordinates of these particles.

Expanding the volume density in spherical harmonics I can write

$$\rho(r, \theta, \phi) = \sum_{l=0}^{\infty} \sum_{m=0}^l P_l^m(\cos \theta) \times [\overline{A_{lm}}(r) \cos(m\phi) + \overline{B_{lm}}(r) \sin(m\phi)], \quad (14)$$

where I have combined terms with opposite sign of m , and where

$$\overline{A_{lm}}(r) = N_{lm} \sum_k \frac{m_k}{r_k^2} \delta(r - r_k) P_l^m(\cos \theta_k) \cos(m\phi_k), \quad (15)$$

$$\overline{B_{lm}}(r) = N_{lm} \sum_k \frac{m_k}{r_k^2} \delta(r - r_k) P_l^m(\cos \theta_k) \sin(m\phi_k), \quad (16)$$

$$N_{lm} = \frac{2l+1}{4\pi} (2 - \delta_{m0}) \frac{(l-m)!}{(l+m)!} \quad (17)$$

and $\delta_{m0}=1$ if $m=0$ and $\delta_{m0}=0$ otherwise. A similar equation can be obtained for the mass within a thin spherical shell, where the $\overline{A_{lm}}(r)$ and $\overline{B_{lm}}(r)$ are replaced by

$$A_{lm}(r) = N_{lm} \sum_k m_k P_l^m(\cos \theta_k) \cos(m\phi_k), \quad (18)$$

and

$$B_{lm}(r) = N_{lm} \sum_k m_k P_l^m(\cos \theta_k) \sin(m\phi_k), \quad (19)$$

and where, as in Eq. 13, the summation is carried over all particles in the shell and where r is the mass-averaged mean radius of

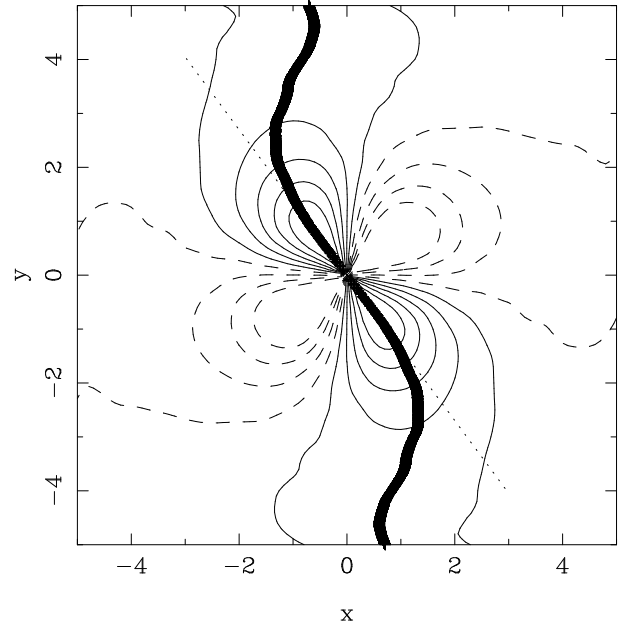


Figure 8. Isocontours of the $l=2$ $m=2$ component of the halo mass distribution on the equatorial plane. Positive isocontours are given with solid lines and negative ones with dashed lines. The thick line shows the phase of the halo bar and the thin dotted line gives the position angle of the disc bar.

the shell. The corresponding amplitudes are equal to $H_{lm}(r) = \sqrt{A_{lm}^2(r) + B_{lm}^2(r)}$ and can be used to measure the halo bar strength (e.g. in Fig. 7 and 9).

The amplitude of the various $l=2$ components is shown, after smoothing, in Fig. 7. The $l=2$, $m=0$ component is linked to the flattening of the halo component towards the disc equatorial plane, while the $l=2$, $m=2$ component is linked to the halo bar contribution, i.e. it would have been zero for an axisymmetric system. It is clear that the $m=2$ component drops faster with distance from the centre and has roughly disappeared at a radius of 4 initial disc scale-lengths, while the $m=0$ component extends more than twice as far. This explains the result found in § 3.2, namely that the halo mass distribution is prolate in the inner parts and oblate in the outer parts and also agrees with the visual impression given by Figs. 2 and 4, namely that the isodensities become axisymmetric before becoming spherical. The $l=0$, $m=4$ stays within the noise, showing that there is no quadrupole component, in good agreement with the ellipse fitting results described in the § 3.2.

The middle panel of Fig. 7 compares the phase of the $l=2$, $m=2$ component with that of the disc bar. A similar comparison can also be made from Fig. 8, which shows the isocontours of this component on the equatorial plane. The two figures, viewed together, show clearly that in the innermost parts the phase of the halo bar does not change much with radius and that its value is similar to that of the disc bar. At larger radii, however, the halo bar phase clearly lags (trails) behind that of the disc bar, the difference in angle increasing considerably with radius. At large distances, the $l=m=2$ component of the halo can be described as a very open trailing spiral. Thus, it will exert a torque on the disc bar and pull it backwards.

To look in more detail at the behaviour of the halo bar in the innermost parts and in particular to get more information on its phase relative to that of the disc bar, I need to average over time, to improve the signal-to-noise ratio. Of course, this can only be done towards the end of the simulation, when the time evolution is

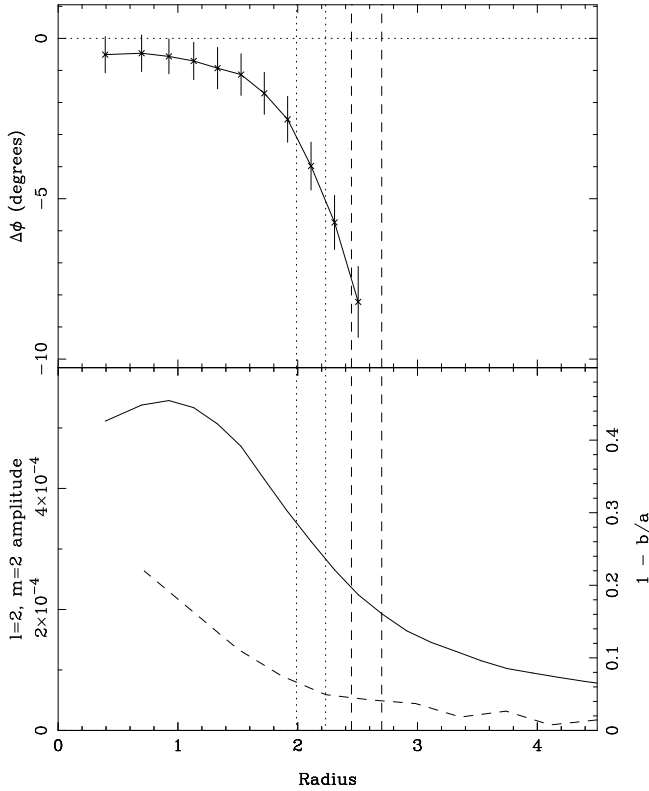


Figure 9. Measuring the halo bar length. The upper panel shows the phase difference between the halo and the disc bar averaged between times $700 < t < 900$, as a function of distance from the centre. The values represent averages over time and the vertical error bars have a length of one σ , as explained in the text. The vertical dotted and dashed lines give the one σ range for the length of the halo bar (see text). The lower panel gives the radial profile of the $l=2, m=2$ amplitude (solid line, ordinate to the left) and of the ellipticity (dashed line, ordinate to the right). The dashed and dotted vertical lines are continuations from the upper panel.

slow. A typical result is shown in Fig. 9, where I have averaged the results of nine equidistant times in the interval $700 < t < 900$. The error bars have a length of one σ and $\Delta\phi$ is measured from the phase of the disc bar. Note that even the innermost point lags behind the disc bar, but with a difference which is less than half a degree. This difference increases with increasing distance from the centre. It is thus not possible to say what the difference between the phases of the disc and the halo bar is and this can well explain the differences between the values quoted in the literature, which are thus not necessarily due to differences between the simulations, but could simply be due to the fact that the measurements were made at different radii. The lengths of the error bars also increase with distance from the centre, but remain reasonably small, at least for simulations where the $l=m=2$ component is sufficiently strong.

Using the results of § 3 and 4, it is possible to define the halo bar length in three different ways. From the change of its phase, or from the radius at which the $l=2, m=2$ amplitude drops to a certain fraction of its maximum, or from the ellipticity $1-b/a$ (see AM02 for corresponding definitions of the disc bar length). All three definitions include a certain amount of arbitrariness, since in the first one needs to define what the maximum allowed phase change is, and in the second one what fraction of the maximum amplitude should be used. Finally, the third method would not be arbitrary if, as in disc galaxies, the ellipticity profile had a clear feature which

one could associate to the bar length. This, however, is not the case for the halo. To illustrate this arbitrariness, I measure the length of the bar by the first definition and a phase difference of 5° (or 10°) and give the results by vertical lines in the upper panel of Fig. 9 for the times used in that figure. The interval between the two dotted (dashed) lines corresponds to one sigma of the bar length measurements and gives an estimate of the increase of the halo bar length during that interval of the evolution. These lines are continued in the lower panel, which shows the radial profile of the $l=2, m=2$ spherical harmonic and of the ellipticity. It is clear that the bar length when measured by the phase shift will be shorter than when measured in the two other ways, since there is a drastic change of the phase with radius at radii at which the amplitude of the $l=2, m=2$ component is still quite high. In fact, measurements from the radial profile of this amplitude, or from the ellipticity will give information on the bar and spiral combined, i.e. give the radial extent of a feature which is much larger than the bar. Thus, the correct way of measuring the halo bar length is from the phase shift. It is interesting to note that this length, as measured by a phase difference of 5° , agrees well with the location at which the triaxiality changes from prolate to oblate (Fig. 5). Since these measurements are made in totally independent ways, this agreement gives confidence that the phase shift gives a relatively accurate estimate of the halo bar length. It also shows clearly that the halo bar is much shorter than the disc bar and that the measurements from the radial profile of the $l=2, m=2$ component would have given an overestimate.

Since the phase of the halo bar is roughly equal to that of the disc bar at all times, the two bars must rotate with roughly the same pattern speed and thus have roughly the same corotation radius. Furthermore, the halo bar is considerably shorter than the disc bar, i.e. it is a slow bar with a corotation radius considerably larger than the bar length.

5 KINEMATICS OF THE HALO COMPONENT

Several N -body simulations have shown that the halo can absorb angular momentum (e.g. Sellwood 1982; Debattista & Sellwood 2000; A02; A03; O'Neill & Dubinski 2003; Valenzuela & Klypin 2003; Martinez-Valpuesta *et al.* 2006). A03 found a correlation between the angular momentum absorbed by the halo and the bar strength (see Figs. 16 and 17 of that paper). One can thus expect some rotation in the halo component of barred galaxies, particularly if the bar is strong, and I will show in this section that this is indeed the case.

Fig. 10 gives information on the kinematics of the halo component. The upper panel shows the rotation curve (i.e. the average tangential velocity for particles within a cylindrical annulus as a function of the radius of the centre of the annulus) for three groups of particles: particles with $|z| < 0.5$, particles with $0.5 < |z| < 1.5$ and particles with $1.5 < |z| < 2.5$. Note that there is important difference between the three, in the sense that particles near the equatorial plane rotate considerably faster than particles further away from it. The particles nearest to the equatorial plane, rotate considerably, with a V_{max} of 0.063 (compared to a V_{max} of 0.77 for the disc component) and a $V_{max}/\sigma_r(R=0)$ of 0.11, where $\sigma_r(R=0)$ is the radial velocity dispersion at the centre. This is well below the oblate rotator line (Binney & Tremaine 1987), which, for an axial ratio of 0.8 and an isotropic velocity dispersion tensor, has a V/σ_r value ~ 0.64 . The rotation curve of this group of particles is not flat. It rises slowly, reaches a maximum at $R=2.1$ and then drops at a rate comparable to that at which it increases

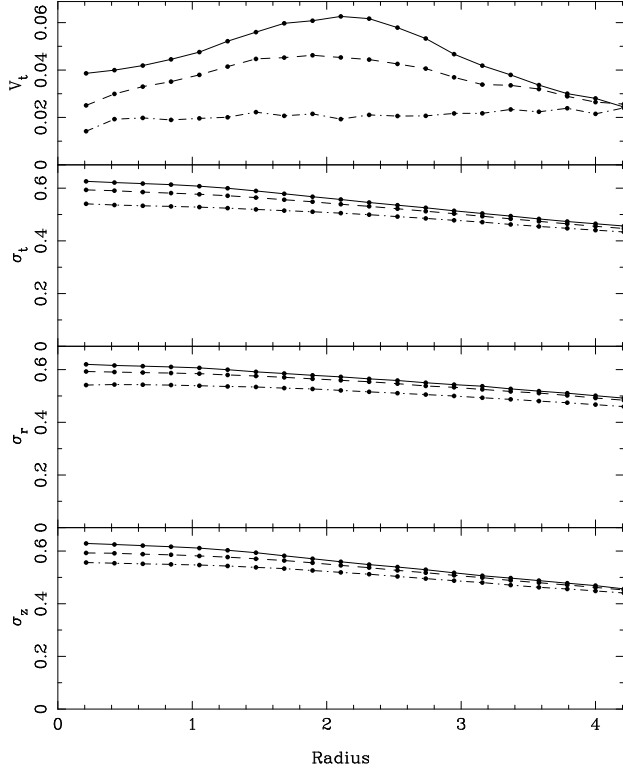


Figure 10. Radial profile of the tangential velocity (upper panel) and tangential (second panel), radial (third panel) and z component (lower panel) of the velocity dispersion, all as a function of cylindrical radius. Particles were split according to their z coordinate. Results for particles very near the equatorial plane ($|z| < 0.5$) are given with a solid line, results for intermediate particles ($0.5 < |z| < 1$) with a dashed line and results for particles further up ($1 < |z| < 2$) with a dot-dashed line.

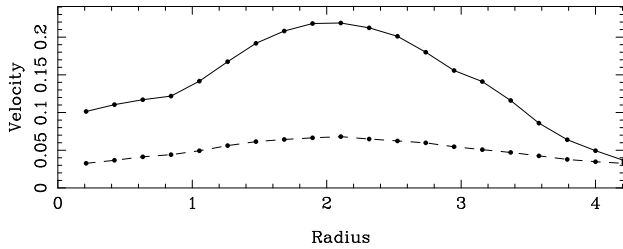


Figure 11. Tangential velocity as a function of cylindrical radius at time 900. Only particles very near the equatorial plane ($|z| < 0.5$) are used. The solid line takes into account all particles that fulfil this criterion for $820 \leq t \leq 900$, while the dashed line takes into account all particles that fulfil this criterion at $t = 900$.

at small radii. The maximum is located much further out than the maximum of the disc circular rotation curve, which is at a radius less than one, and is comparable to the halo bar length (see § 4). Similar remarks can be made also for particles in the intermediate $|z|$ bin.

The values of the rotational velocity are even bigger if, instead of using all particles which at the time of the measurement have a $|z| < 0.5$, I take all particles that fulfil this condition at all times in a given time interval. This is clear from Fig. 11, which compares the rotation curve from all particles that have $|z| < 0.5$ at $t = 900$, with the rotation curve obtained from particles that have $|z| < 0.5$ at all times $820 \leq t \leq 900$. Note that the latter has a maximum ve-

locity more than three times higher than the former. The reasons for this are going to be discussed further in Paper II. It should be noted, however, that even these particles have a considerably smaller rotational velocity than the disc particles.

The lower three panels of Fig. 10 show the three components of the velocity dispersion. All three have a maximum at the centre, as expected, and decrease with increasing radius. By comparing them, one can see that the halo has a velocity distribution not far from isotropic. The three curves in each panel were obtained by binning particles by their $|z|$, as for the tangential velocity (upper panel). It is clear that particles with higher $|z|$ give larger σ values, but the difference is not as large as for the tangential velocity.

6 SUMMARY

A bar is not the monopoly of the disc component; such a structure is also found in the halo of strongly barred galaxies. It has been called the halo bar (here), or the dark matter bar (Colin *et al.* 2006). I make here a detailed analysis of the properties of a fiducial model. As the disc bar, the halo bar can be found in the inner parts of the galaxy and it is roughly centred on the galaxy centre. Using the inertia tensor, I calculated its axial ratios and found that it is triaxial with the short axis along the axis of rotation. It is most elongated at the innermost parts, with an axial ratio of the order of .8, and turns gradually to spherical with increasing distance from the centre. Using two different measures of the triaxiality, I show that the halo mass distribution is prolate-like out to a certain radius and oblate-like beyond that. I also looked at its shape using ellipse fits, in a way analogous to the disc bar, in order to make comparisons. I show that the equatorial plane ellipticity decreases gradually with distance from the centre, but has no sharp drop to provide a measurement of the halo bar length.

I expand the halo density in spherical harmonics and analyse the properties of the $l = 2$ and $l = 4$ components. The $l = 2$, $m = 2$ component decays faster than the $l = 2$, $m = 0$ one, explaining the fact that the halo mass distribution is prolate in the inner parts and oblate further out. The amplitude of the $l = 4$, $m = 0$ component is considerably smaller (about a factor of three or four) than that of the $l = 2$, $m = 0$. Spherical harmonics also provide a measurement of the halo bar phase. I find that in the centermost part the halo bar lags the disc bar by very little (of the order of a degree), but that the difference increases with increasing distance from the centre, initially slower and then considerably faster. It becomes larger than 5° at distances somewhat larger than 2 initial disc scale-lengths. This, and in particular the isocontours of the $l = 2$, $m = 2$ component, show that the halo deformation is indeed bar-like in the inner parts and becomes spiral-like further out, always lagging behind the disc bar. I use the phase of the $l = 2$, $m = 2$ component to measure the bar length, and find that the end of the bar roughly coincides with the position where the triaxiality, as measured from the inertia tensor, turns from prolate to oblate. Since these two measurements are done in a completely independent way, this agreement gives me confidence that I am measuring correctly the halo bar length. The amplitude of the $l = 2$, $m = 2$ component is large even beyond the end of the bar and this can be understood by the fact that beyond the bar there is a spiral of considerable amplitude.

I also analyse the kinematics of the halo component and find that there is indeed some rotation, although it is largely constrained to a layer around the equatorial plane. The maximum of the rotation occurs not far from the end of the halo bar. The velocity dispersion is not far from isotropic. It also decreases with distance from the

equatorial plane, but the effect is much less than for the tangential velocity. The V/σ value shows that the halo is a slow rotator.

A general discussion of the implications of the results presented in this paper will come after Paper II. In that paper I will apply the techniques introduced here to a large sample of several hundred simulations, with different initial conditions described in § 2, and I will make comparisons and statistics. I will also discuss the time evolution of the various halo bar properties and parameters.

There is a general qualitative agreement between our results and those presented in previous studies mentioned in the Introduction. The comparison, however, can only be fragmentary, since there is no previous complete study covering all the aspects of the halo properties considered here. Furthermore, a quantitative comparison is not possible at this stage, since, as I will show in Paper II, there are considerable differences from one model to the other and many properties show trends as a function of the model parameters.

ACKNOWLEDGEMENTS

I thank A. Bosma, A. Misiriotis and K. Holley-Bockelmann for many useful discussions and/or email exchanges and Jean-Charles Lambert for computing assistance. I also thank the INSU/CNRS, the region PACA and the University of Aix-Marseille I for funds to develop the computing facilities used for the simulations discussed in this series of paper. This work started while I was visiting INAOE. I would like to thank ECOS-Nora and ANUIES for financing this trip and my collaborators in INAOE for their kind hospitality.

REFERENCES

- Aguilar, L. A., Merritt, D. 1990, *ApJ*, 354, 33
 Athanassoula, E., 1996, in “Barred Galaxies”, eds. R. Buta, D. Crocker and B. Elmegreen, PASP conference series, 91, 309
 Athanassoula, E. 2002, *ApJ*, 569, L83 (A02)
 Athanassoula, E. 2003, *MNRAS*, 341, 1179 (A03)
 Athanassoula, E., 2004, in “Dark Matter in Galaxies”, eds. S. Ryder, D. J. Pisano, M. Walker & K. C. Freeman, IAU symposium series, 220, 255
 Athanassoula, E. 2005a, *MNRAS*, 358, 1477
 Athanassoula, E. 2005b, *Cel. Mech. & Dyn. Astr.*, 91, 9
 Athanassoula, E. 2005c, in “Nonlinear Dynamics in Astronomy and Physics (In memory of Henry E. Kandrup)”, eds. S. T. Gottesman, J.-R. Buchler and M. E. Mahon, *Annals of the New York Academy of Sciences*, 1045, 168 and *astro-ph/0504664*
 Athanassoula, E., Misiriotis, A. 2002, *MNRAS*, 330, 35 (AM02)
 Athanassoula, E., Morin, S., Wozniak, H., Puy D., Pierce M., Lombard J., Bosma A., 1990, *MNRAS*, 245, 130
 Barnes J. E., 1988, *ApJ*, 331, 699
 Barnes J. E., 1992, *ApJ*, 393, 484
 Berentzen, I., Shlosman, I. 2006, *ApJ*, 648, 807
 Berentzen, I., Shlosman, I., Jogee, S. 2006, *ApJ*, 637, 582
 Binney, J. Tremaine, S. 1987, *Galactic Dynamics*, Princeton University press
 Boily, C. M., Athanassoula, E., 2006, *MNRAS*, 369, 608
 Buta, R., Laurikainen, E., Salo, H., Block, D. L., Knapen, J. H. 2006, *AJ*, 132, 1859
 Casertano, S., Hut, P. 1985, *ApJ*, 298, 80
 Ceverino, D., Klypin, A. 2005, *astro-ph/0503710*
 Colin, P., Valenzuela, O. Klypin, A. 2006, *ApJ*, 644, 687
 Cuddeford P., 1991, *MNRAS*, 253, 414
 Debattista, V. P., Mayer, L., Carollo, M. Moore, B., Wadsley, J., Quinn, T. 2006, *ApJ*, 645, 209
 Debattista, V. P., Sellwood, J. A. 2000, *ApJ*, 543, 704
 Dehnen, W. 1999, *AJ*, 118, 1201
 Dehnen, W. 2000, *ApJL*, 536, L39
 Dehnen, W. 2002, *Journal of Computational Physics*, 179, 27+
 El-Zant, A., Shlosman, I. 2002, *ApJ*, 577, 626
 Fuchs, B. 2004, *A&A*, 419, 941
 Fuchs, B., Athanassoula, E. 2005, 444, 455
 Heller, C., Shlosman, I., Athanassoula, E. 2007, *ApJL*, 657, L65
 Hernquist, L. 1990, *ApJ*, 356, 359
 Hernquist, L. 1993, *ApJS*, 86, 389
 Hernquist, L., Weinberg, M. D. 1992, *ApJ*, 400, 80
 Holley-Bockelmann, K., Weinberg, M. D., Katz, N., 2005, *MNRAS*, 363, 991
 Kalnajs, A. J. 1971, *ApJ*, 166, 275
 Kawai, A., Fukushima, T., Makino, J., Taiji, M. 2000, *PASJ*, 52, 659
 King, I. R. 1966, *AJ*, 71, 64
 Kormendy, J. 1979, *ApJ*, 227, 714
 Kuijken, K., Dubinski, J. 1994, *MNRAS*, 269, 13
 Kuijken, K., Dubinski, J. 1995, *MNRAS*, 277, 1341
 Kuijken, K., Tremaine, S. 1992, in “Dynamics of Disk Galaxies”, ed. B. Sundelius, Göteborg University press, Göteborg, p. 341
 Laurikainen, E., Salo, H., Buta, R., Knapen, J. H., Speltin, T., Block, D. L. 2006, *AJ*, 132, 1859
 Little, B., Carlberg, R. G. 1991a, *MNRAS*, 250, 161
 Little, B., Carlberg, R. G. 1991b, *MNRAS*, 251, 227
 Lynden-Bell, D., Kalnajs, A. J. 1972, *MNRAS*, 157, 1, 1972
 Mark, J. W.-K. 1976, *ApJ*, 206, 418
 Martinez-Valpuesta, I., Shlosman, I. 2004, *ApJ*, 613, 29
 Martinez-Valpuesta, I., Shlosman, I., Heller, C. 2006, *ApJ*, 637, 214
 McMillan, P. J., Athanassoula, E., Dehnen, W. 2007, *MNRAS*, in press and *astro-ph/0701541*
 McMillan, P. J., Dehnen, W. 2005, *MNRAS*, 363, 1205
 McMillan, P. J., Dehnen, W. 2007, *MNRAS*, submitted
 Ohta, K. 1996, in ASP conference Series Vol 91, Barred Galaxies, eds. R. Buta, D. A. Crocker, B. G. Elmegreen, (San Francisco: ASP), 37
 Ohta, K., Hamabe, M., Wakamatsu, K. 1990, *ApJ*, 357, 71
 O’Neill, J. K., Dubinski, J. 2003, *MNRAS*, 346, 251
 Sellwood, J. A. 1980, *A&A*, 89, 296
 Sellwood, J. A. 2003, *ApJ*, 587, 638
 Sellwood, J. A. 2006, *astro-ph/0610468*
 Shu, F. H. 1969, *ApJ*, 158, 505
 Sygnet, J. F., Tagger, M., Athanassoula, E., Pellat, R. 1988, *MNRAS*, 232, 733
 Tagger, M., Sygnet, J. F., Athanassoula, E., Pellat, R. 1987, *ApJL*, 318, L43
 Teuben P.J. 1995 in “Astronomical Data Analysis Software and Systems IV”, ed. R. Shaw, H. E. Payne and J. J. E. Hayes, ASP conference series, 77, 398
 Toomre, A. 1964, *ApJ*, 139, 1217
 Tremaine, S., Ostriker, J. P. 1999, *MNRAS*, 306, 662
 Tremaine, S., Weinberg, M. D. 1984, *MNRAS*, 209, 729
 Weinberg, M. D. 1985, *MNRAS*, 213, 451
 Weinberg, M. Katz N. 2002, *ApJ*, 580, 627
 Valenzuela, O., Klypin, A. 2003, *MNRAS*, 345, 406